RSC Advances

PAPER

View Article Online
View Journal | View Issue

Cite this: *RSC Adv.*, 2024, **14**, 36416

Optimization of $CsPbBr_3$/PVDF composite for enhanced UV photodetection application†

Amr Elattar, *[a] Okenwa Okoli [ab] and Tarik Dickens*[a]

Received 14th October 2024
Accepted 9th November 2024

DOI: 10.1039/d4ra07369j

rsc.li/rsc-advances

Halide perovskites have exhibited great research impact for developing innovative materials with novel properties. Here, we report the synthesis of different caesium lead bromide perovskites using different (Cs/Pb) molar ratios and fabrication of their corresponding perovskite/polyvinylidene fluoride (PVDF) composites, as well as study of their structural and UV-photodetection properties. Spin-coated perovskite/PVDF composite thin films revealed strong oriented XRD diffraction peaks along the *c*-axis direction (00l) with homogeneously distributed perovskite microcrystals in the polymer matrix. The high-Cs containing perovskite/PVDF composite, with Cs/Pb (3/1) molar ratio, demonstrated the highest green emission under UV light and its corresponding UV-photodetector exhibited the highest UV photo-responsivity. These results highlight the importance of structural modulation and additive manufacturing for tailoring the optoelectronic properties of halide perovskites.

Introduction

Halide perovskite materials have attracted great attention in various optoelectronic fields owing to their high absorption coefficient,[1] long carrier diffusion length,[2–4] and tunable bandgap.[5–10] 3D $CsPbBr_3$ perovskite, which belongs to the Cs–Pb–Br material system, is considered one of the most common halide perovskites with substantial potential for light-emitting diodes,[11–15] photodetectors,[16] scintillators,[17–23] and laser applications.[24–27] In general, the Cs–Pb–Br material system has two further thermodynamically stable related-perovskite phases rather than the orthorhombic $CsPbBr_3$ perovskite phase: the 2D Pb-rich $CsPb_2Br_5$ and the 0D Cs-rich Cs_4PbBr_6 which have tetragonal and trigonal crystal structures, respectively.[28,29] The Cs–Pb–Br perovskites have green emission with different photoluminescence (PL) properties.[30–35] Recently, it was found that the different PL behaviour of $CsPb_2Br_5$ and Cs_4PbBr_6 is due to the formation of large/weak and small/strong $CsPbBr_3$ nanocrystals (NCs) embedded through $CsPb_2Br_5$ and Cs_4PbBr_6 matrices, respectively.[36]

The Cs–Pb–Br material systems have been devoted to photodetection applications as single crystals,[37] bulk polycrystalline thin films[38–41] and nanocrystal-based thin films.[42–49] In general, regarding the perovskite thin films, the deposition of halide perovskites *via* solution processing results in the formation of polycrystalline films with structural defects at the grain boundaries. These defects induce the formation of non-radiative recombination centers, limiting optoelectronic device efficiency.[50] Perovskite-polymer composites are supposed to be one of the most effective strategies to modulate the perovskite crystallinity and minimize the formation of structural defects.[51,52] Poly(vinylidene fluoride) (PVDF) polymer has piqued the interest of researchers to be introduced as a polymer matrix to host perovskite materials to enhance their stability and crystallinity owing to strong hydrophobic fluorine (F) atoms in PVDF matrix, which can form coordinate bonds with Pb^{2+} and strong hydrogen bonds with organic cations.[53] Sultana *et al.* reported higher stability, piezoelectric, and photodetection properties of $MAPbI_3$/PVDF composite compared to pristine $MAPbI_3$.[54] Moreover, Zhu group demonstrated the flexible piezoelectric devices with enhanced stability of black γ-phase $CsPbI_3$ through embedding in PVDF matrix.[55] Furthermore, Sun *et al.* showed 24% efficiency of $FAMAPb(I/Br)_3$/PVDF composite-based perovskite solar cell with an excellent V_{oc} value (1.22 V).[53]

These findings motivate us to explore the influence of incorporating PVDF matrix on the structural and photodetection properties of Cs–Pb–Br perovskite systems, targeting improved crystallinity and structural defect mitigation in perovskite thin film processing for enhanced photodetection performance. Herein, PVDF matrix enhances the perovskite film coverage and the perovskite film crystallinity. Moreover, the performance of photodetection properties is in the order of 0D Cs_4PbBr_6 > 3D $CsPbBr_3$ > 2D $CsPb_2Br_5$ perovskite/PVDF composite-based devices.

Experimental

Materials

All chemicals were from Sigma-Aldrich unless otherwise noted. Chemicals used were: caesium bromide (CsBr), 99%; lead

[a]*Industrial & Manufacturing Engineering, FAMU-FSU College of Engineering, 2525 Pottsdamer St., Tallahassee, Florida, 32310, USA. E-mail: aelattar@fsu.edu; dickens@eng.famu.fsu.edu*

[b]*Herff College of Engineering, University of Memphis, Memphis, TN, 38111, USA*

† Electronic supplementary information (ESI) available. See DOI: https://doi.org/10.1039/d4ra07369j

bromide ($PbBr_2$), 99%; poly(vinylidene fluoride (PVDF) 99%; tin oxide, 15% in H_2O colloidal dispersion from Alfa Aesar. *N*,*N*-dimethylformamide (DMF), 99% and dimethylsulfoxide (DMSO), were used as solvents. Indium-doped tin oxide (ITO) substrates were used for fabrication of photodetector devices. Isopropanol, 99% was used for cleaning substrates. Helman III from Hellmax Analytics, nano pure water, and acetone were additionally used for cleaning substrates.

Synthesis of perovskites and perovskites/PVDF composites

As shown in Table 1, four different caesium lead bromide perovskite powders were prepared *via* mortar grinding of different ($CsBr/PbBr_2$) mole ratios for 15 min. Their corresponding perovskite solutions were prepared by dissolving 100 mg perovskite powder in 1 mL DMSO under stirring at 90 °C for 60 min. For the synthesis of perovskite/PVDF composite solutions, 100 mg perovskite powder was dissolved with 100 mg of PVDF pellets in 2 mL DMF/DMSO 1 : 1 (v/v) mixed solvents under stirring at 120 °C for 120 min. Both perovskite and perovskite/PVDF composite thin films were fabricated *via* spin-coating 100 μL of the above-mentioned solutions over pre-cleaned ozone-treated ITO substrates at 1200 rpm for 30 s. After that, substrates were annealed at 80 °C for 15 min.

Fabrication of perovskite/PVDF-based photodetectors (PDs)

Etching of ITO substrates *via* zinc powder and hydrochloric acid (HCl) followed by cleaning *via* Helman detergent, deionized water, acetone, and isopropanol, respectively, under sonication for 15 min for each solvent. Finally, ITO substrates were treated with ozone-plasma for 15 min. For electron transport layer (ETL), 200 μL of 15% SnO_2 in H_2O was dropped over ITO. They were spun at 1000 rpm for 5 s and then at 4500 rpm for 30 s. After spin-coating, ITO/SnO_2 substrates were annealed at 120 °C for 30 min then treated with ozone-plasma for 15 min. After that, perovskite/PVDF composite thin films were fabricated with the same procedure as mentioned above. Finally, carbon metal contact was printed over composite layer through doctor blading of carbon paste with annealing at 80 °C for 20 min.

Characterization

The X-ray diffraction (XRD) measurements for powder perovskites and composite thin films were performed by the Rigaku Smart lab diffractometer. The morphological structures of perovskite crystal and composite thin film were studied using scanning electron microscopy (SEM, Thermo Fisher). The current–time (*I*–*t*) and the current–voltage (*I*–*V*) characteristics of the UV photodetector were measured by Keithley 2400 system source meter that was attached to a computer through a GPIB 488A interface. For UV light illumination, a Sinus-70 solar simulator (WAVELABS Solar Metrology Systems GmbH) was used for measuring the photo-response of the fabricated ITO/SnO_2/perovskite–PVDF composite/Carbon device. The photocurrent-time characteristic curves were measured under UV lamp (365 nm) with power intensity (100 mW cm^{-2}). All measurements were performed under ambient atmosphere.

Table 1 Mole ratios of raw materials used for preparing caesium lead bromide perovskite powders

CsBr (mol)	$PbBr_2$ (mol)	Perovskite abbreviation
1	1	X1
1	2	X2
3	1	X3
4	1	X4

Results and discussion

Four different molar ratios of $CsBr/PbBr_2$ are utilized to prepare caesium lead bromide perovskites, as depicted in Table 1; X1 has equimolar Cs/Pb precaursors, X2 has a higher Pb content, and X3–X4 have higher Cs content with 3/1 and 4/1 Cs/Pb ratios, respectively. Generally, the four grinded perovskites showed the similar orange color under white light, as shown in Fig. 1a, where X1–X2 samples exhibited darker orange. However, the higher Cs-containing samples X3–X4 exhibited more lighter orange color. Under UV light, as shown in Fig. 1b, the equimolar perovskite sample powder X1 exhibited less green emission, whereas the higher Pb-containing sample powder X2 exhibited no green emission. On the other hand, X3–X4 samples have the highest green emission which revealed the critical role of Cs/Pb mor ratio to modulate the green emission under UV.

Most of perovskite-based photodetector devices are fabricated using solution-processed perovskites rather than solid-based perovskites. As a result, we studied the effect of perovskite solution processing on the green emission under UV. Fig. 1c and d show the similar behaviour of all DMSO/perovskite solutions under both white and UV lights where the colorless perovskite solutions have the same low green emission. This reveals the demolishing of the impact of different Cs/Pb molar ratios which has a negative effect towards commercialization of perovskite-based devices.

Morphological cubic structure of caesium lead bromide was confirmed microscopically by scanning electron microscopy (SEM), as shown in Fig. 1e. The homogeneous distribution of Cs, Pb, and Br elements in lead-based perovskite structure is also confirmed *via* the elemental mapping of EDS, as depicted in Fig. 1f. To characterize the different caesium lead bromide perovskite powders, we obtained the X-ray diffraction data (Fig. 1g). High Cs-containing perovskites, X3 and X4, have shown nearly similar XRD patterns. XRD plots of X1, X2, and X3–X4 perovskites show three different diffraction peaks, suggesting their possession of different crystal structures. Generally, caesium lead bromide perovskite has three different crystal structures, as depicted in ESI Fig. S1.† $CsPbBr_3$, $CsPb_2Br_5$, and Cs_4PbBr_6 perovskites have orthorhombic, tetragonal, and trigonal crystal structures, respectively. Rietveld XRD refinement was performed for perovskite samples to determine their corresponding crystal structures, as shown in ESI Fig. S2.† Table 2 depicts the weight % of different phases of each perovskite sample. It was found that all samples have multiphases. X1, X2, and X3-X4 samples have a major phase of $CsPbBr_3$, $CsPb_2Br_5$, and Cs_4PbBr_6 crystal structures, respectively, with the existence

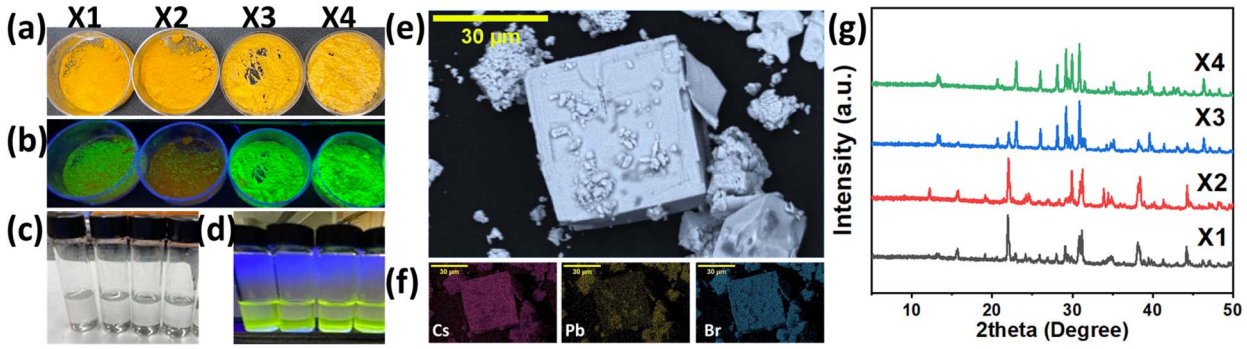

Fig. 1 Different caesium lead bromide perovskite powders prepared *via* grinding method: (a) under white light. (b) Under UV light. Their corresponding perovskites dissolved in DMSO (c) under white light. (d) Under U.V. light. (e) Scanning Electron Microscope (SEM) images of $CsPbBr_3$ perovskite. (f) Elemental mapping of perovskite elements: Cs, Pb, and Br. (g) Powder XRD patterns of caesium lead bromide perovskite powders.

of the other phases as minor contents. To overcome the appearance of multiphases of perovskite powders and the demolishing of green emission under UV for their corresponding solutions as well, perovskite/PVDF composites were prepared through dissolving the composite in DMF/DMSO mixed solvents where PVDF is easily dissolved in DMF while perovskite is easily dissolved in DMSO. It was found that perovskite/PVDF composite solutions maintained their green emission variance, as shown in Fig. 2a. This observation reveals the impact of PVDF polymer on perovskite stability through DMF/DMSO mixed solvents. Compared to spin-coated perovskites (Fig. 2b and d), spin-coated perovskite/PVDF composite thin films show homogeneous distribution of perovskite microcrystals through PVDF polymer with uniform and fully covered surfaces without any voids (Fig. 2c and e). The composite formation was confirmed microscopically by SEM, as shown in Fig. 2f, where perovskite microcrystals are distributed through PVDF polymer matrix. Elemental mapping of EDS revealed the homogeneous distribution of F and Pb elements (Fig. 2g) which correspond to PVDF and perovskite, respectively. XRD patterns, as shown in Fig. 2h, revealed the high orientation along *c*-axis direction (00l) of perovskite crystals embedded through PVDF polymer. It is worth mentioning that XRD peak of PVDF polymer at $2\theta = 20.3°$ disappeared through the XRD patterns of the composite thin films.[56] This might be attributed to the high crystallinity of homogeneously distributed perovskite microcrystals through the amorphous polymer clusters which resulted in hindering XRD peak of PVDF polymer. Strong diffraction peaks of X1 perovskite at 15.4° and 30.9° are related to (002) and (004) lattice planes, respectively. This result is consistent with the orthorhombic structure of $CsPbBr_3$.[57]

Table 2 Estimation of weight%, obtained from Rietveld refinement, of possible phases for each perovskite sample

Samples	$CsPbBr_3$	$CsPb_2Br_5$	Cs_4PbBr_6
X1	86.8%	3.3%	9.9%
X2	2.8%	56.7%	40.5%
X3	13.7%	7.9%	78.4%
X4	17.3%	28.2%	54.5%

Furthermore, X2 perovskite showed the tetragonal structure pattern of $CsPb_2Br_5$ perovskite with diffraction peaks at 11.8°, 23.6°, 35.7°, and 48.1° corresponded to (002), (004), (006), and (008) planes, respectively.[28] On the other hand, X3 and X4 perovskites with similar diffraction peak positions at 20.8° and 42.2°, related to (004) and (006) lattice planes, confirms their trigonal structure of Cs_4PbBr_6 perovskite.[29] As a result, the presence of PVDF polymer matrix induces the formation of perovskite single phase, rather than the multi phases of pristine perovskites. This might be assigned to the high electronegativity of Fluoride and Oxygen through PVDF where the Lewis acid of Pb^{2+} interacts with the Lewis base of PVDF through coordination bonds to increase the perovskite nucleation rate as well as to form a single perovskite phase through nucleation sites depending on Cs/Pb precursor.[58] The observations demonstrate that the assembly of lead bromide perovskites produced from perovskite/PVDF composite solution is parallel to the glass substrate surface with a spacing between consecutive Pb-inorganic layers of 5.8 Å, 7.0 Å, and 8.6 Å for X1, X2, and X3–X4 perovskites, respectively, as depicted in Fig. 3a–c, respectively. Furthermore, it is worth noting that the composite formation has no impact on the crystal structure of X1(Fig. 3d). However, the X2 perovskite shows strained crystal structure (Fig. 3e). On the other hand, crystal structure of X3 and X4 samples reveal compression effect upon composite formation (Fig. 3f).

The perovskite/PVDF-based photodetectors (Fig. 4a), with cell configuration of ITO/SnO_2/perovskite–PVDF/carbon, are studied by current–voltage (*I–V*) characteristics in the dark and under UV illumination, measured at room temperature. Fig. 4b–e depicts the typical *I–V* curves of the X1, X2, X3, and X4 photodetectors, respectively, at the dark and at different UV light power intensities (25%, 50%, 75%, and 100%) of total power intensity (100 mW cm^{-2}). It is obvious that the as-prepared X2-based photodetector shows the highest dark current (Fig. S3†) with a negligible photocurrent enhancement upon UV illumination (Fig. 4c). This might be attributed to the presence of both high and low concentrations of tetragonal and orthorhombic structures of $CsPb_2Br_5$ and $CsPbBr_3$ perovskites, respectively, through X2 composite matrix. Meanwhile, X4-

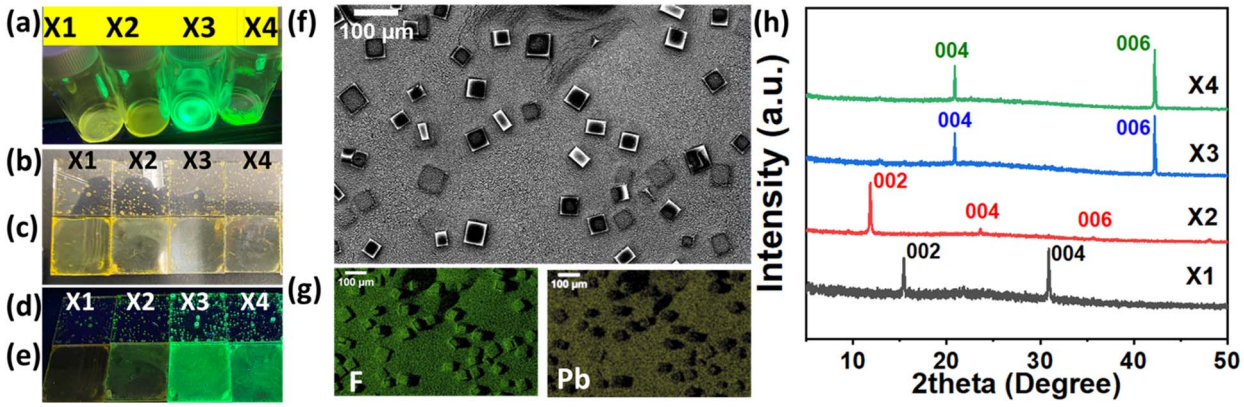

Fig. 2 (a) Perovskite/PVDF composites in (DMF/DMSO) mixed solvents under UV light. (b and d) Spin-coated thin films of perovskites only, and (c and e) perovskite/PVDF composites, under white and UV lights, respectively. (f) (SEM) images of $CsPbBr_3$/PVDF composite thin film and (g) its F and Pb elemental mapping. (h) XRD patterns of caesium lead bromide perovskites/PVDF composites thin films.

based sample exhibit higher UV-response (Fig. 4e) than X2 which might be assigned to the existence of higher and lower concentrations of orthorhombic and tetragonal structures of $CsPbBr_3$ and $CsPb_2Br_5$ perovskites, respectively. X1 (Fig. 4b) and X3 (Fig. 4d)-based devices depict a significant responsivity for UV illumination which might be ascribed to their containing of the lowest concentration of $CsPb_2Br_5$ tetragonal structure. Generally, it can be clearly found that tetragonal structure of $CsPb_2Br_5$ perovskite has a negative impact on the photo-detection application. However, high concentrations of $CsPbBr_3$ and Cs_4PbBr_6 perovskites, with orthorhombic and trigonal structures, have a positive effect towards higher photodetectivity.

(On/Off) time-resolved photo-current response measurement has been conducted at zero bias voltage within time intervals (10 seconds) under alternating dark and different UV light power intensities (25%, 50%, 75%, and 100%) of total power intensity (100 mW cm^{-2}). Fig. 4f–i exhibit time-resolved photo-response [(I–t) curves] of X1, X2, X3, and X4-based photodetectors, respectively. All perovskite samples show photo-current response under (On/Off) UV illumination which corroborates their photodetection tendency. It is worth noting that as the UV light power intensity increases, the absorption of UV photons increases and the difference between dark and photo-current increases, as well.

The results above are further supported by a detailed performance comparison among the different perovskite/PVDF composites-based devices, as shown in Table 3, where X3-based device is considered the best fabricated perovskite/PVDF composite-based photodetector. Various parameters were calculated, as shown in ESI notes 1,† where the photodetector effective area was 4.25 cm^2 for all fabricated devices. The

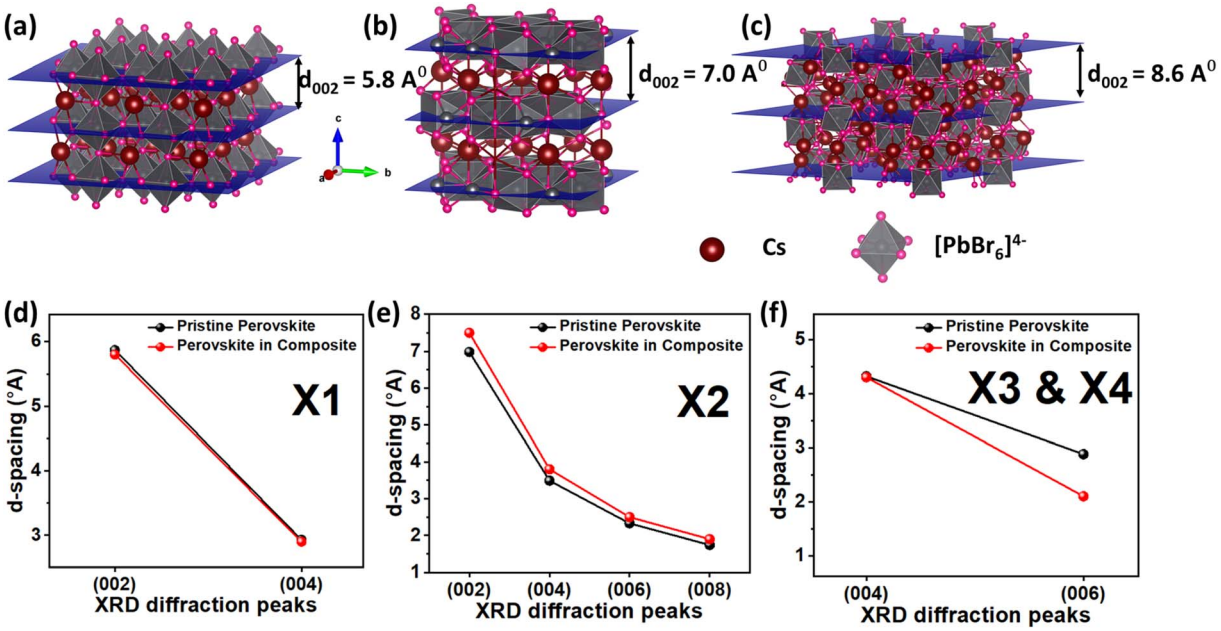

Fig. 3 Crystal structures (a–c) and change in d-spacing (d–f) of X1, X2, and X3–X4 perovskites embedded in PVDF polymer, respectively.

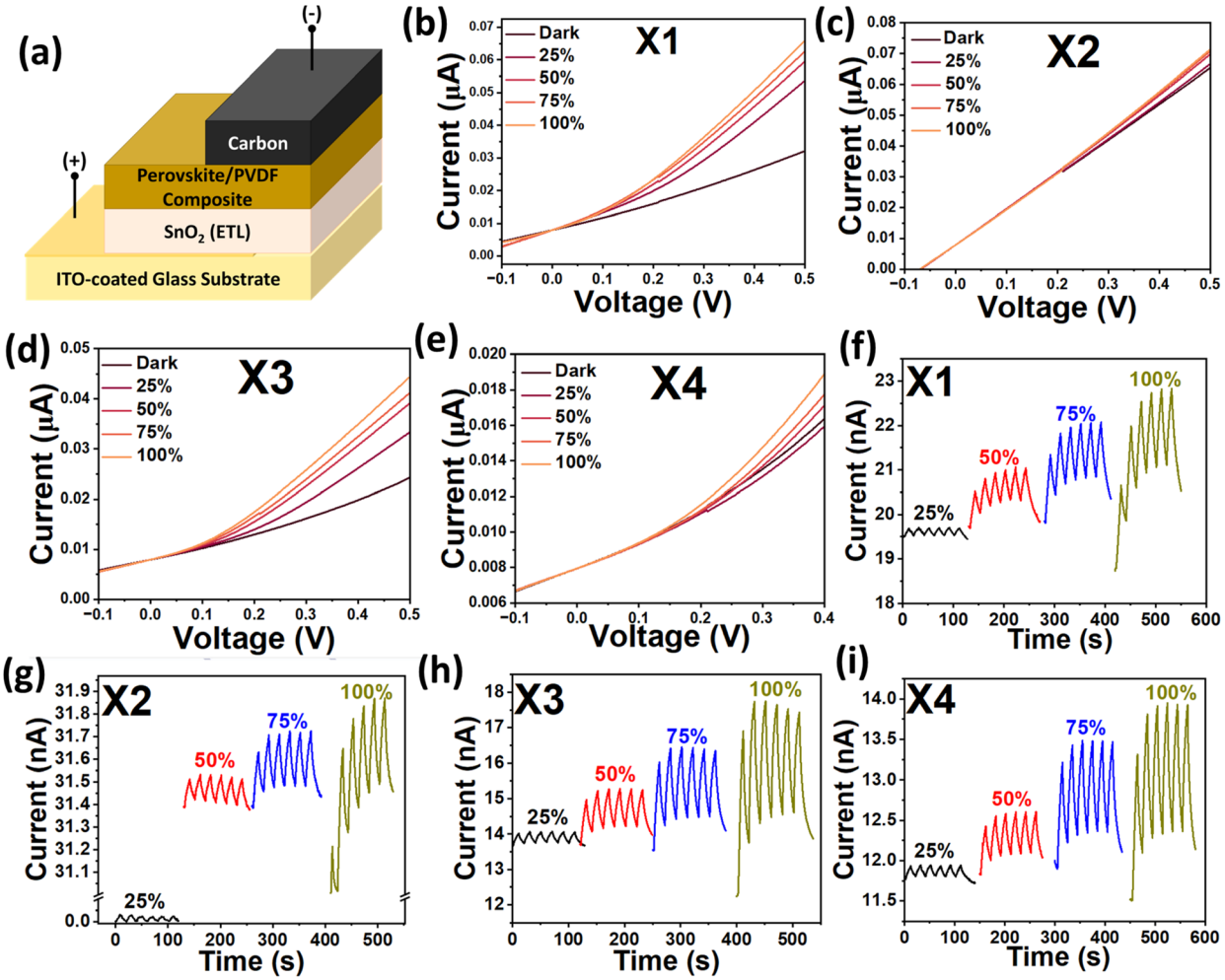

Fig. 4 Perovskite/PVDF-based photodetector cell configuration (a). The current–voltage *I*–*V* curves (b–d) and the transient *I*–*t* (ON/OFF) curves (e–i) of the devices of different caesium lead bromide perovskites/PVDF composites-based photodetectors under different UV light intensities: (dark, 25%, 50%, 75%, and 100%).

Table 3 Photodetector properties of different PVDF/perovskite-based UV-photodetection devices

Perovskite/PVDF PDs	Photoresponsivity R_λ (nA W^{-1})	Photosensitivity ξ	Quantum efficiency IQE $\times 10^{-6}$ (%)	Detectivity $D^* \times 10^4$ (Jones)
X1	4.24	0.0861	1.441	337.63
X2	1.07	0.0145	0.363	69.53
X3	7.40	0.2171	2.514	708.11
X4	3.80	0.1310	1.292	394.34

photoresponsivity (R_λ) of X1, X2, X3, and X4-based devices were estimated to be 4.24, 1.07, 7.40, and 3.80 nA/W, respectively. The photosensitivity (ξ) was found to be 0.0861, 0.0145, 0.2171, and 0.1310 for X1, X2, X3, and X4-based photodetectors, respectively. The efficiency of the carrier transport through photodetector was estimated with calculating the internal quantum efficiency (IQE). The IQE of X1, X2, X3, and X4-based photodetectors were found to be 1.441 $\times$ 10^{-6}%, 0.363 $\times$ 10^{-6}%, 2.514 $\times$ 10^{-6}%, and 1.292 $\times$ 10^{-6}%, respectively. Finally, the photodetector quality was tracked *via* calculating of detectivity (D^*) which was estimated to be 337.63 $\times$ 10^4 Jones, 69.53 $\times$ 10^4 Jones, 708.11 $\times$ 10^4 Jones, and 394.34 $\times$ 10^4 Jones, for X1, X2, X3, and X4-based photodetectors, respectively. The best photodetection performance of X3 device might be assigned to the higher photoluminescence quantum yield (PLQY), longer PL lifetime, and higher exciton binding energy of 0D-Cs_4PbBr_6, compared to 2D $CsPb_2Br_5$ and 3D $CsPbBr_3$ perovskites.[59,60]

Conclusions

In summary, caesium lead bromide perovskites with different crystal structures have been synthesized *via* mortar grinding of different ratios of CsBr and $PbBr_2$. It was found that higher Cs

content enhances the green emission of the as-prepared perovskite. Compared to pristine perovskite, spin-coating of perovskite/PVDF composites has a substantial impact on both the film coverage and the orientation of perovskite microcrystals formed through PVDF matrix. The existence of single phase of trigonal Cs_4PbBr_6 through perovskite/PVDF composite thin film was found to enhance the overall photodetection parameters.

Data availability

The data supporting this article has been included as part of the ESI.†

Author contributions

Amr Elattar conceived the idea for the manuscript, designed the experiments, conducted characterizations, and wrote the first manuscript. All authors discussed the results and commented on the manuscript at all stages. Okenwa Okoli and Tarik Dickens led the project and provided editing.

Conflicts of interest

There are no conflicts to declare.

Acknowledgements

Authors acknowledge the NNSA MSIPP I-AM EMPOWER'D (Grant No. DE-NA0004004) at the FAMU-FSU College of Engineering, Dr Siegrist lab for XRD usage, and the DOW SURE program for donation of desktop SEM program.

Notes and references

1 X. Du, J. Li, G. Niu, J.-H. Yuan, K.-H. Xue, M. Xia, W. Pan, X. Yang, B. Zhu and J. Tang, *Nat. Commun.*, 2021, **12**, 3348.
2 Y. Chen, H. T. Yi, X. Wu, R. Haroldson, Y. N. Gartstein, Y. I. Rodionov, K. S. Tikhonov, A. Zakhidov, X.-Y. Zhu and V. Podzorov, *Nat. Commun.*, 2016, **7**, 12253.
3 S. Shrestha, X. Li, H. Tsai, C.-H. Hou, H.-H. Huang, D. Ghosh, J.-J. Shyue, L. Wang, S. Tretiak, X. Ma and W. Nie, *Chem*, 2022, **8**, 1107–1120.
4 J. Lim, M. Kober-Czerny, Y.-H. Lin, J. M. Ball, N. Sakai, E. A. Duijnstee, M. J. Hong, J. G. Labram, B. Wenger and H. J. Snaith, *Nat. Commun.*, 2022, **13**, 4201.
5 S. A. Kulkarni, T. Baikie, P. P. Boix, N. Yantara, N. Mathews and S. Mhaisalkar, *J. Mater. Chem. A*, 2014, **2**, 9221–9225.
6 D. B. Straus and R. J. Cava, *ACS Appl. Mater. Interfaces*, 2022, **14**, 34884–34890.
7 M. R. Filip, G. E. Eperon, H. J. Snaith and F. Giustino, *Nat. Commun.*, 2014, **5**, 5757.
8 Y. Li, T. Yang, Y. She, B. Xu, Y. Du and M. Zhang, *Inorg. Chem.*, 2023, **62**, 19248–19255.
9 R. J. Sutton, G. E. Eperon, L. Miranda, E. S. Parrott, B. A. Kamino, J. B. Patel, M. T. Hörantner, M. B. Johnston, A. A. Haghighirad, D. T. Moore and H. J. Snaith, *Adv. Energy Mater.*, 2016, **6**, 1502458.
10 E. L. Unger, L. Kegelmann, K. Suchan, D. Sörell, L. Korte and S. Albrecht, *J. Mater. Chem. A*, 2017, **5**, 11401–11409.
11 W. Zheng, Q. Wan, M. Liu, Q. Zhang, C. Zhang, R. Yan, X. Feng, L. Kong and L. Li, *J. Phys. Chem. C*, 2021, **125**, 3110–3118.
12 S.-R. Bae, M. J. Seol and S. Y. Kim, *Nanoscale*, 2023, **15**, 9533–9542.
13 C.-T. Li, K.-L. Lee, S.-F. Wang and L.-C. Chen, *J. Mater. Res. Technol.*, 2023, **22**, 375–381.
14 H. Liu, T. B. Shonde, O. J. Olasupo, M. S. Islam, T. F. Manny, M. Woodhouse, X. Lin, J. S. R. Vellore Winfred, K. S. Mao, E. Lochner, I. Fatima, K. Hanson and B. Ma, *ACS Energy Lett.*, 2023, **8**, 4259–4266.
15 L.-C. Chen and C.-H. Kao, *Sci. Rep.*, 2022, **12**, 14750.
16 G. Xiong, G. Zhang and W. Feng, *Mater. Res. Bull.*, 2024, **179**, 112959.
17 V. B. Mykhaylyk, H. Kraus, V. Kapustianyk, H. J. Kim, P. Mercere, M. Rudko, P. Da Silva, O. Antonyak and M. Dendebera, *Sci. Rep.*, 2020, **10**, 8601.
18 F. Cova, A. Erroi, M. L. Zaffalon, A. Cemmi, I. Di Sarcina, J. Perego, A. Monguzzi, A. Comotti, F. Rossi, F. Carulli and S. Brovelli, *Nano Lett.*, 2024, **24**, 905–913.
19 V. Naresh, S. Singh, H. Soh, J. Lee and N. Lee, *Mater. Today Nano*, 2023, **23**, 100364.
20 M. Baravaglio, B. Sabot, F. Maddalena, M. D. Birowosuto, C. Dang, C. Dujardin and B. Mahler, *Nanoscale*, 2024, **16**, 17176–17186.
21 T. Skrypnyk, O. Viahin, I. Bespalova, O. Zelenskaya, V. Tarasov, V. Alekseev, S. Yefimova and O. Sorokin, *Radiat. Meas.*, 2023, **169**, 107028.
22 J. Ghosh, J. O'Neill, M. G. Masteghin, I. Braddock, C. Crean, R. Dorey, H. Salway, M. Anaya, J. Reiss, D. Wolfe and P. Sellin, *ACS Appl. Nano Mater.*, 2023, **6**, 14980–14990.
23 Z.-W. Lü, G.-X. Wei, H.-Q. Wang, Y. Guan, N. Jiang, Y.-Y. Liu, Z. Li, H. Qin and H.-Q. Liu, *Nucl. Sci. Tech.*, 2022, **33**, 98.
24 J. Tian, G. Weng, Y. Liu, S. Chen, F. Cao, C. Zhao, X. Hu, X. Luo, J. Chu, H. Akiyama and S. Chen, *Commun. Phys.*, 2022, **5**, 160.
25 C.-Y. Huang, C. Zou, C. Mao, K. L. Corp, Y.-C. Yao, Y.-J. Lee, C. W. Schlenker, A. K. Y. Jen and L. Y. Lin, *ACS Photonics*, 2017, **4**, 2281–2289.
26 J. Huang, Y. Zhong, T. Guo, K. Qian and J. Li, *J. Lumin.*, 2024, **272**, 120650.
27 S. Guo, C. Li, H. Jia and N. Li, *ACS Omega*, 2022, **7**, 45504–45509.
28 V. Drushliak and M. Szafrański, *Inorg. Chem.*, 2022, **61**, 14389–14396.
29 M. De Bastiani, I. Dursun, Y. Zhang, B. A. Alshankiti, X.-H. Miao, J. Yin, E. Yengel, E. Alarousu, B. Turedi, J. M. Almutlaq, M. I. Saidaminov, S. Mitra, I. Gereige, A. AlSaggaf, Y. Zhu, Y. Han, I. S. Roqan, J.-L. Bredas, O. F. Mohammed and O. M. Bakr, *Chem. Mater.*, 2017, **29**, 7108–7113.

30 M. A. P. Gómez, J. S. Rodríguez-Hernández, B. S. Araújo, W. C. Ferreira, C. W. A. Paschoal and A. P. Ayala, *J. Phys. Chem. C*, 2024, **128**, 6821–6828.
31 Z.-L. Yu, Y.-Q. Zhao, Q. Wan, B. Liu, J.-L. Yang and M.-Q. Cai, *J. Phys. Chem. C*, 2020, **124**, 23052–23058.
32 B. Turedi, K. J. Lee, I. Dursun, B. Alamer, Z. Wu, E. Alarousu, O. F. Mohammed, N. Cho and O. M. Bakr, *J. Phys. Chem. C*, 2018, **122**, 14128–14134.
33 G. Maity and S. K. Pradhan, *J. Alloys Compd.*, 2020, **816**, 152612.
34 S. Caicedo-Dávila, H. Funk, R. Lovrinčić, C. Müller, M. Sendner, O. Cojocaru-Mirédin, F. Lehmann, R. Gunder, A. Franz, S. Levcenco, A. V. Cohen, L. Kronik, B. Haas, C. T. Koch and D. Abou-Ras, *J. Phys. Chem. C*, 2019, **123**, 17666–17677.
35 Z.-P. Huang, B. Ma, H. Wang, N. Li, R.-T. Liu, Z.-Q. Zhang, X.-D. Zhang, J.-H. Zhao, P.-Z. Zheng, Q. Wang and H.-L. Zhang, *J. Phys. Chem. Lett.*, 2020, **11**, 6007–6015.
36 S. Caicedo-Dávila, P. Caprioglio, F. Lehmann, S. Levcenco, M. Stolterfoht, D. Neher, L. Kronik and D. Abou-Ras, *Adv. Funct. Mater.*, 2023, **33**, 2305240.
37 P. Cheng, Z. Liu, R. Kang, J. Zhou, X. Wang, J. Zhao and Z. Zuo, *ACS Omega*, 2023, **8**, 26351–26358.
38 M. Xue, H. Zhou, G. Ma, L. Yang, Z. Song, J. Zhang and H. Wang, *Sol. Energy Mater. Sol. Cells*, 2018, **187**, 69–75.
39 A. Perveen, S. Hussain, Y. Xu, A. Raza, F. Saeed, N. Din, A. Subramanian, Q. Khan and W. Lei, *J. Photochem. Photobiol., A*, 2022, **426**, 113764.
40 Y. Li, Z.-F. Shi, S. Li, L.-Z. Lei, H.-F. Ji, D. Wu, T.-T. Xu, Y.-T. Tian and X.-J. Li, *J. Mater. Chem. C*, 2017, **5**, 8355–8360.
41 F. Hua, X. Du, Z. Huang, Y. Gu, J. Wen, F. Liu, J. Chen and T. Tang, *J. Mater. Chem. C*, 2024, **41**, 55–61.
42 H. Zhou, R. Wang, X. Zhang, B. Xiao, Z. Shuang, D. Wu and P. Qin, *IEEE Trans. Electron Devices*, 2023, **70**, 6435–6438.
43 K. Shen, H. Xu, X. Li, J. Guo, S. Sathasivam, M. Wang, A. Ren, K. L. Choy, I. P. Parkin, Z. Guo and J. Wu, *Adv. Mater.*, 2020, **32**, 2000004.
44 L. Zhu, X. Cheng, A. Wang, Y. Shan, X. Cao and B. Cao, *Appl. Phys. Lett.*, 2023, **123**, 212105.
45 B. Moon, J.-H. Ahn, M.-H. Jeong, S.-H. Lee and J.-S. Lee, *Adv. Opt. Mater.*, 2023, **11**, 2300414.
46 D.-H. Kwak, D.-H. Lim, H.-S. Ra, P. Ramasamy and J.-S. Lee, *RSC Adv.*, 2016, **6**, 65252–65256.
47 C. H. Kang, I. Dursun, G. Liu, L. Sinatra, X. Sun, M. Kong, J. Pan, P. Maity, E.-N. Ooi, T. K. Ng, O. F. Mohammed, O. M. Bakr and B. S. Ooi, *Light Sci. Appl.*, 2019, **8**, 94.
48 R. Wang, H. Zhou, B. Wu, D. Wu, L. Tao, H. Wang, X. Peng, J. Zhang and H. Wang, *J. Phys. Chem. Lett.*, 2021, **12**, 7519–7525.
49 B. Yang, W. Bi, F. Jin, X. Ma and S.-Q. Guo, *Compos. Commun.*, 2022, **29**, 101032.
50 Y. Zong, Y. Zhou, Y. Zhang, Z. Li, L. Zhang, M.-G. Ju, M. Chen, S. Pang, X. C. Zeng and N. P. Padture, *Chem*, 2018, **4**, 1404–1415.
51 B. Niu, H. Wu, J. Yin, B. Wang, G. Wu, X. Kong, B. Yan, J. Yao, C.-Z. Li and H. Chen, *ACS Energy Lett.*, 2021, **6**, 3443–3449.
52 Q. Fu, Z. Xu, X. Tang, T. Liu, X. Dong, X. Zhang, N. Zheng, Z. Xie and Y. Liu, *ACS Energy Lett.*, 2021, **6**, 1521–1532.
53 R. Sun, Q. Tian, M. Li, H. Wang, J. Chang, W. Xu, Z. Li, Y. Pan, F. Wang and T. Qin, *Adv. Funct. Mater.*, 2023, **33**, 2210071.
54 A. Sultana, P. Sadhukhan, M. M. Alam, S. Das, T. R. Middya and D. Mandal, *ACS Appl. Mater. Interfaces*, 2018, **10**, 4121–4130.
55 W. Zhu, A. A. Khan, M. M. Rana, R. Gautheron-Bernard, N. R. Tanguy, N. Yan, P. Turban, S. Ababou-Girard and D. Ban, *ACS Omega*, 2022, **7**, 10559–10567.
56 X. Cai, T. Lei, D. Sun and L. Lin, *RSC Adv.*, 2017, **7**, 15382–15389.
57 M. Rodová, J. Brožek, K. Knížek and K. Nitsch, *J. Therm. Anal. Calorim.*, 2003, **71**, 667–673.
58 Y. Ren, Y. Hao, N. Zhang, Z. Arain, M. Mateen, Y. Sun, P. Shi, M. Cai and S. Dai, *Chem. Eng. J.*, 2020, **392**, 123805.
59 X. Chen, D. Chen, J. Li, G. Fang, H. Sheng and J. Zhong, *Dalton Trans.*, 2018, **47**, 5670–5678.
60 M. I. Saidaminov, J. Almutlaq, S. Sarmah, I. Dursun, A. A. Zhumekenov, R. Begum, J. Pan, N. Cho, O. F. Mohammed and O. M. Bakr, *ACS Energy Lett.*, 2016, **1**, 840–845.